Research Square

Preprints are preliminary reports that have not undergone peer review.
They should not be considered conclusive, used to inform clinical practice,
or referenced by the media as validated information.

Reciprocating-Disc-type Magnetorheological Finishing with Long-term Removal-function Stability

Jiyi Jiang

24110367@bjtu.edu.cn

beijing jiaotong daxue jixie yu dianzi kongzhi gongcheng xueyuan: Beijing Jiaotong University School of Mechanical Electronic and Control Engineering

Zhili Zhang
Jiwen Li
Yue Zhang
Tao Zhang
Decai Li

Research Article

Keywords: magnetorheological polishing, ultra-precision machining, nano tribology, K9 glass

Posted Date: August 7th, 2026

DOI: https://doi.org/10.21203/rs.3.rs-10085829/v1

License: This work is licensed under a Creative Commons Attribution 4.0 International License.
Read Full License

Reciprocating-Disc-type Magnetorheological Finishing with Long-term Removal-function Stability

Jiyi Jiang[1], Zhili Zhang[1,*], Jiwen Li[1], Yue Zhang[1], Tao Zhang[1], Decai Li[2]

1. School of Mechanical Electronic and Control Engineering, Beijing Jiaotong University, Beijing, 100044, China
2. State key laboratory of tribology in advanced equipment, Tsinghua University, Beijing, 100084, China

Jiyi Jiang 24110367@bjtu.edu.cn
Zhili Zhang zlzhang@bjtu.edu.cn

Abstract

The well known Disc-type magnetorheological finishing (DMRF) has damage-free advantage due to "surface contact" during polishing process. It has got more attention from integrated circuit (IC) industry to obtain wafer-level ultra-smooth planarization and other fields requiring ultra-precise surface processing. However, conventional DMRF configurations exhibiting unstable material removal rate (MRR) which constrain their application, one reason is the variation of the linear speed of the disc polishing surface, the another is evaporation of water in magnetorheological polishing fluid (MRPF) during polishing. To obtain stable material removal rate (MRR), a kind of reciprocating-disc-type magnetorheological finishing (RDMRF) equipment is designed and practiced in our experiment, and the effect factors contributing to drift in removal-function accuracy are identified and discussed, including influence of time. MRPF with sodium-hexametaphosphate (SHAMP) and vapor-deposited silica was used in polishing, and the results showed that the shear stress rises by 47 % and sedimentation rate falls by 57 % compared with pure magnetorheological fluid. Using this MRPF can achieve a surface roughness of Sa 1.562 nm on workpieces. A Preston-type model integrating workpiece elastic modulus and magnetic-field gradient is established. In order to avoid instability caused by temperature and evaporation, a magnetically actuated recovery loop was constructed to provide on-the-fly replenishment and continuous agitation of the MR fluid. With this loop engaged, the material-removal-rate drift was suppressed to <8 % over 180 min and the areal roughness Sa converged to 1.519 nm. Deviation is caused by minute fluctuations in the composition of the slurry during the polishing process. This reveals the root cause limiting the stability of removal and further improvement in surface quality.

Keywords: magnetorheological polishing; ultra-precision machining; nano tribology; K9 glass

1. Introduction

Nowadays, the goals of photonic and semiconductor manufacturing are increasingly approaching the millimeter-scale features and sub-nanometer surface finish[1,2]. Float polishing, elastic-emission machining and ion-beam figuring routinely deliver atomic-scale roughness, but their removal rates are typically <10 nm min^{-1}. Large-area substrates therefore demand processing times of several days, excluding these techniques from high-throughput manufacturing lines[3,4]. Magnetorheological finishing(MRF), introduced by Kordonski, exploits the magnetorheological effect to generate a compliant, abrasive-bearing tool for deterministic surface correction[5]. Under the gradient magnetic-field, carbonyl-iron particles and nanometric abrasives assemble into a viscoelastic "flexible wheel" whose yield stress is controlled by the local flux density. The workpiece material is removed at near-ambient temperature as the wheel drags abrasives across the surface in a rolling–ploughing mode; because the penetration depth remains below the brittle–ductile transition, lattice distortion and micro-cracking are suppressed[6,7]. Wheel and ball-end magnetorheological polishers continue to rely on sub-aperture, point-by-point scanning. A millimeter-scale tool must execute dense, overlapping X–Y raster strokes to cover the entire surface, so processing time scales quadratically with aperture diameter and wafer-level batches cannot be finished within production takt times[8].

Recent academic efforts have migrated from pursuiting of ultimate precision toward simultaneous optimization both of precision and throughput. Ren[10] introduced the Belt-MRF architecture to replace the conventional wheel with a compliant belt polishing brush. Operated under the same magnetic field and MR fluid, the belt platform raises the volumetric removal rate of SiC by approximately 5 times, while preserving a stable removal function and rapid convergence, and it provided a practical route for metre-class (>2 m) precision optics. However, the unidirectional kinematics of the belt imprint a pronounced lay pattern on the surface, limitted to obtain further roughness and quality. Owing to its full-face, contactless material-removal paradigm and verified absence of subsurface damage,Disc-type magnetorheological finishing (DMRF) is currently regarded as the most manufacturable route for wafer-level ultra-smooth planarization that concurrently satisfies throughput and surface-integrity specifications. Pan et al.[11] formulated a Preston-based removal model for magnetic-field-cluster DMRF that explicitly incorporates workpiece elastic modulus and field gradient, enabling quantitative, damage-free polishing of 6H-SiC and Si wafers deformed within the elastic–plastic regime. Bai et al.[12] showed that the viscoelastic envelope generated by magnetorheological clustering in DMRF traps oversized loose abrasives, suppressing indentation damage and enabling defect-free, angstrom-level finishing of brittle optical materials. Lu et al.[13] presented an instantaneous micro-abrasive disc that exploits the magnetorheological effect; a closed magnetic circuit secures a spatially uniform abrasive flux, raising both removal rate and surface

finish when planarising brittle substrates. Jiang et al.[15] introduced a permanent-magnet disc MRF configuration that enlarges the fluid–workpiece contact zone to boost removal rate. Systematic mapping of gap distance, abrasive volume fraction, and relative rotation speed revealed the parametric windows that drive both efficiency and roughness; coated surfaces were finished from Ra 3.19 nm to 0.293 nm without subsurface alteration. Guo[15,16] advanced a magnetically compounded-fluid (MCF) model under rotating dynamic fields and identified shear-controlled removal as the dominant mechanism, enabling optical-glass finishing at the nanometer scale without detectable damage and at elevated rates. Viney Ghai et al.[17] introduced chemical–mechanical magnetorheological composite (CMMRF) polishing on a disc platform; a brittle in-situ film and compliant magnetic brush cut Al 7075-T6 roughness to Ra 0.597 nm in one pass, >60 % below diamond-turning + CMP and reflectivity +5 %, enabling atomic-scale finishing of aluminum optics.

In our experiment, we found that orbital–rotational kinematics imposes a radial velocity gradient that leaves DMRF with non-uniform removal and unchecked long-term drift. Therefore, a reciprocating-disc protocol is introduced to enrich the trajectory and to quantify removal-function stability over extended process windows. Addition to it, a accessory recovery device of continuous replenishment and agitation of the MR fluid with magnetic field actuated was constructed, in order to avoid instability of fluid caused by temperature.

2. Equipment and Experimental Procedures

2.1 Operating Principle and Instrumentation of RDMRF

The schematic of the RDMRF system is presented in Fig.1(a). It consists of a polishing disc rotating about its own axis, a workpiece clamped in a fixture and driven separately, a permanent-magnet array located beneath the disc, and a magnetorheological fluid whose active region remains stationary relative to the disc. Reciprocal movement is executed by the workpiece spindle. The permanent magnets are arranged in a Halbach array, a configuration that concentrates the magnetic flux on the fluid side while cancelling the field on the back side, thereby doubling the effective flux density in the polishing gap. The vertical separation between the workpiece lower face and the polishing-disc upper face is defined as the processing gap, h; the distance from the workpiece lower face to the upper face of the magnet array is designated the excitation gap, σ. At the onset of polishing, carbonyl-iron particles within the magnetorheological fluid polarized along the field lines to form rigid chains (Figure 1(b)); nanometric abrasives are trapped at the apex of these chains immediately beneath the workpiece. The superimposed field gradient and relative motion generate a localized normal force that presses the abrasives against the surface, inducing micro-cutting. A magnified view of the active layer is provided in Figure 1(c). The entrapped abrasives transmit normal stress σ<sub> and tangential stress σ<sub> to the workpiece. Micromechanical analysis shows that the magnetic chains impose shear within the fluid, nucleating micro-cracks at surface asperities; these cracks

propagate under continued contact until the protrusions fracture and are swept away. Importantly, the chains themselves do not apply direct shear to the bulk workpiece surface.

Figure 1(d) depicts the physical layout of the excitation unit—a Halbach permanent-magnet array (N52 grade)—together with three-dimensional magnetic-field simulations at 5 mm, 6 mm and 7 mm lift distances. Figure 1(e) shows the magnetorheological polishing fluid beneath the permanent-magnet array; under the field the fluid solidifies into a stable, geometrically defined polishing film.

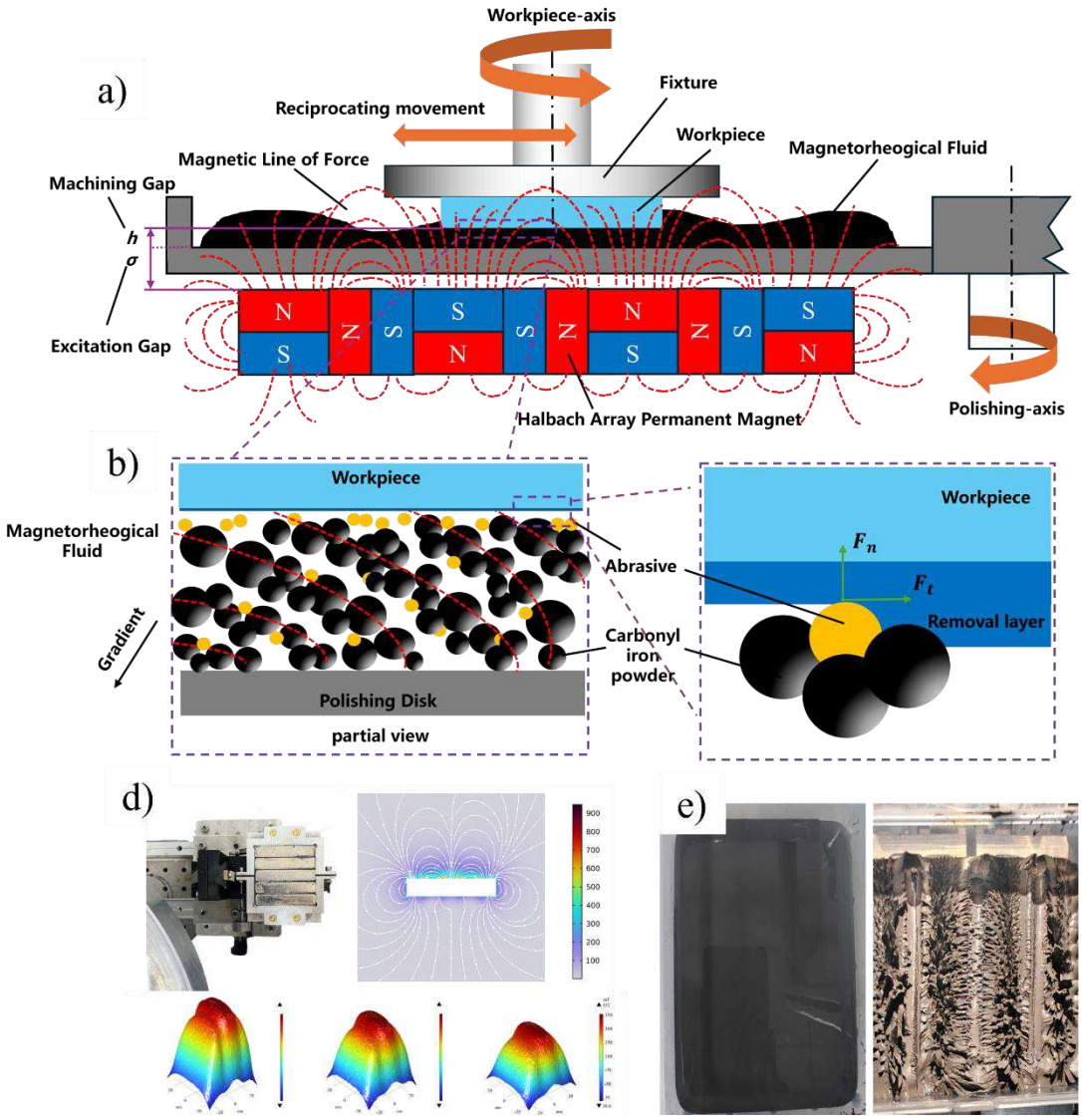

Fig.1 Key Components and Schematic Diagram of Reciprocating Disc-Type Magnetorheological Finishing(RDMRF)

(a)Schematic Diagram of RDMRF (b) Schematic Diagram of RDMRF Shear Process (c) Microscopic Magnification of Shear (d) Physical diagram of Halbach array and COMSOL 3D magnetic field simulation (at distances of 5 mm, 6 mm, and 7 mm) (e) MRPF with and without magnetic field excitation

2.2 Establishment of a Mathematical Model for RDMRF Material Removal

The removal function of RDMRF is governed by the polishing-fluid properties, workpiece topography and hardness, and the applied magnetic field. The model invokes seven simplifying premises: (i) carbonyl-iron and CeO_2 particles are monodisperse spheres; (ii) both of the particles remain uniformly suspended in de-ionized water without sedimentation; (iii) chemical interaction between CeO_2 and the workpiece is negligible; (iv) field-induced iron chains form a regular lattice that evenly traps ceria particles; (v) initial surface topography does not alter ceria contact statistics; (vi) Brownian motion and particle–fluid adhesion are ignored; (vii) the slurry of MRF is supplied in excess.

2.2.1 Modified Preston equation

In conventional polishing, normal pressure and relative linear velocity between pad and surface jointly govern material removal[18]. To improve removal-rate fidelity, a material-specific correction factor is embedded in the classical Preston equation, yielding[19,20]:

$$MRR = Kn\frac{{F_{ni}}^{0.75}}{d_{Abr}}\frac{E^{0.8}}{K_{Ic}H_v^2}PV \tag{3}$$

Symbols: K, Preston coefficient; n, micro-grinding-brush geometry factor; F_{ni}, normal force per abrasive grain; d_{Abr}, mean abrasive diameter; F_n, resultant load; V, relative velocity; E, Young's modulus; K_{Ic}, fracture toughness; H_v, Vickers hardness. The final three are material-specific constants.

2.2.2 Normal-Force Analysis of the Workpiece

Within the hybrid-lubrication framework, the workpiece is subject to three radial contributions: (i) magnetic normal pressure P_n from the gradient field, (ii) hydrodynamic pressure P_d generated by the confined fluid motion, and (iii) buoyancy P_f acting on the submerged volume[11]. Therefore, the total dynamic pressure within the polishing contact area can be expressed as:

$$F_n = P_n + P_f + P_d \tag{4}$$

Among these, the buoyancy force P_f is negligible.

(1) Magnetic normal pressure P_n on the workpiece surface.

The magnetic normal pressure on the workpiece surface increases steeply with decreasing machining gap. The magneto strictive pressure P_n is expressed as[21,22]:

$$P_n = \frac{B_m^2}{4\mu_0} \cdot \left(1 - \frac{3(2+\mu_c)}{3(2+\mu_c)+\pi(\mu_c-1)\varphi}\right) \tag{5}$$

Symbols: μ_0, permeability of free space; μ_c, permeability of carbonyl-iron powder; H, magnetic field strength; t, residence time; v, relative velocity. The gradient-field-averaged pressure on the workpiece, $\overline{P_N}$, is then:

$$\overline{P_N} = \frac{v}{s^2}\int_0^s \frac{B_m^2}{4\mu_0} \cdot \left(1 - \frac{3(2+\mu_c)}{3(2+\mu_c)+\pi(\mu_c-1)\varphi}\right) ds \tag{6}$$

$$\overline{P_N} = \frac{3\pi v B_m^2(\mu_c-1)\varphi}{8s\mu_0[3(2+\mu_c)+\pi(\mu_c-1)\varphi]} \tag{7}$$

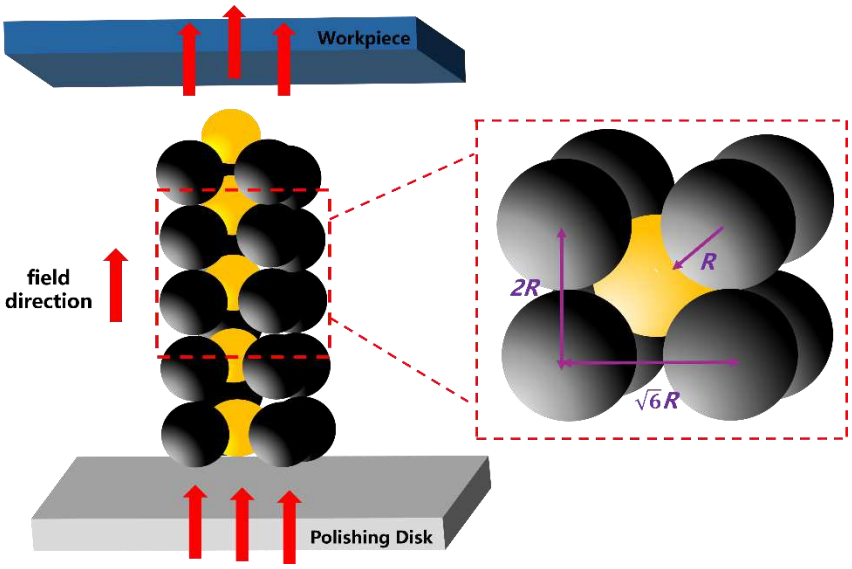

Fig.2 Schematic of body-centered-cubic microstructure formed in high-concentration MRPF under magnetic field

At high particle concentration the carbonyl-iron chains gripping the abrasives are approximated by a body-centered-cubic lattice, illustrated in Fig.2. Assuming a body-centered-cubic lattice of parameter $\sqrt{6}R$ is uniformly distributed beneath the circular contact of radius r_h, the total number of abrasive particles in contact with the workpiece, n_a, is expressed as:

$$n_a = \frac{\pi r_h^2}{6R^2} \tag{8}$$

The normal pressure imposed by one abrasive grain on the workpiece surface is expressed as:

$$P_n = \frac{\overline{P_N}}{n_a} = \frac{9vB_m^2R^2(\mu_c-1)\varphi}{4s\mu_0 r_h^2[3(2+\mu_c)+\pi(\mu_c-1)\varphi]} \tag{9}$$

(2) Hydrodynamic pressure on the workpiece

During magnetorheological polishing, the fluid operates within a magnetically saturated regime.

Under saturation, the magnetorheological fluid behaves as a ferrofluid; its constitutive relation takes the form:

$$\tau(H,D) = \tau_s(H) + \left[\sum_{k=1}^{n} \eta_k(H) \left|\frac{\partial u}{\partial y}\right|^{k-1}\right] \frac{\partial u}{\partial y} \tag{10}$$

Owing to the sub-millimeter polishing film, the field variation across the process zone is negligible and the yield stress is effectively uniform. The viscous contribution is therefore omitted, and the dynamic pressure is governed solely by the second-viscosity coefficient, i.e., the fluid density; the ferrofluid viscosity η_0 is written as:

$$\eta_0 = \frac{\mu}{1 - 2.5\emptyset + 155\emptyset^2} \tag{11}$$

Here μ is the viscosity of de-ionized water and $\emptyset$ the volume fraction of solid particles. As the magnetic brush traverses the workpiece, the magnetorheological fluid satisfies the one-dimensional Reynolds equation for hydrodynamic pressure generation, subject to the boundary conditions: (1) $y_1 = 0$, $v = V$; (2) $y_2 = h$, $v = 0$. With h denoting the machining gap, substitution into the Reynolds equation gives[23]:

$$\frac{\partial P_f}{\partial x} = \frac{6\eta_0 \Delta h}{h^3} \cdot V_Q \tag{12}$$

Substituting (9) into (10) and assuming a uniform array magnetic field, integration yields the hydrodynamic pressure of the MRPF:

$$P_f = \frac{6\eta_0 \Delta h V_Q s}{h^3(1 - 2.5\emptyset + 155\emptyset^2)} \tag{13}$$

2.2.3 Relative-velocity analysis between MRPF and workpiece surface

The kinematics of the RDMRF configuration are illustrated in Figure 3. The velocity of any surface point *Q* relative to the local fluid is the vector sum of the workpiece tangential velocity V_w, the corresponding disc velocity V_d, and the reciprocating velocity V_{rm} imposed on the workpiece.

$$V_w = 2\pi\omega_1 a, \quad V_d = 2\pi\omega_2 b \tag{14}$$

Since the velocity V_w must be perpendicular to *QOw*, only the decomposition of V_d into its *x*- and y-components V_{dx} and V_{dy} is required:

$$V_{dx} = 2\pi\omega_2 b sin\theta, \quad V_{dy} = 2\pi\omega_2 b cos\theta \tag{15}$$

The combined-velocity components in the x and y directions are：

$$V_x = V_w + 2\pi\omega_2 b\sin\theta,\ \ V_y = V_{rm} + 2\pi\omega_2 b\cos\theta \tag{16}$$

The relative velocity follows as：

$$V = \sqrt{(V_w + 2\pi\omega_2 b\sin\theta)^2 + (V_{rm} + 2\pi\omega_2 b\cos\theta)^2} \tag{17}$$

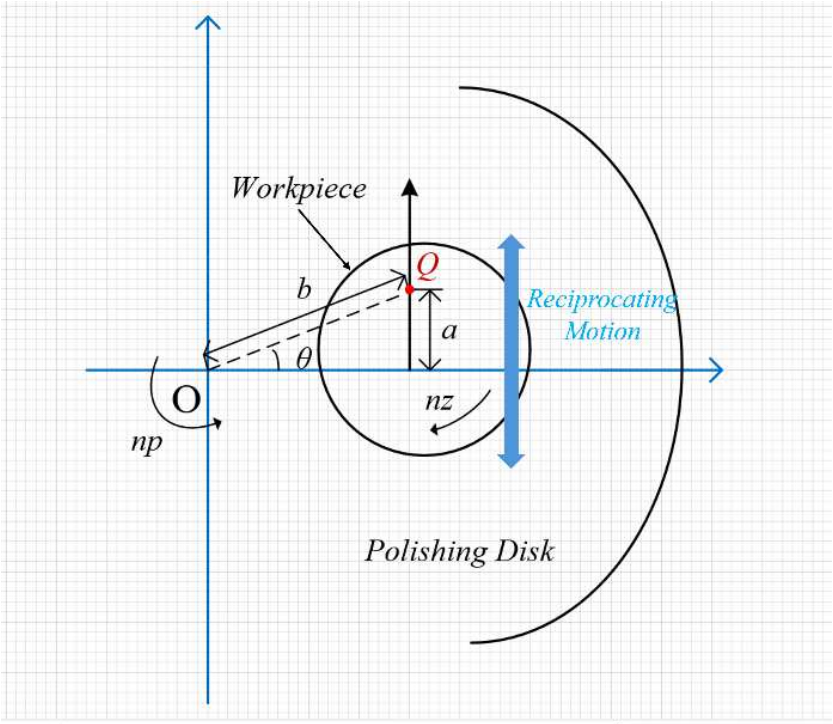

Fig.3. Kinematic schematic of RDMRF

The relative velocity varies periodically with the rotation angle across the workpiece surface. Calculation results show that the maximum percentage variation of velocity induced by the rotating polishing disc is about 6.6%. This indicates that the reciprocating motion effectively suppresses the radial velocity gradient caused by the polishing disc in conventional DMRF.

Substituting expressions (4), (7), (9), (13), and (17) into expression (3) yields the removed function equation.

2.3 Preparation of MRPF

The MRPF is the most important for MRF, prolonged removal stability can only be obtained with a formulation that mirrors the theoretical assumptions and resists drift for extended periods. For ideal MRPF, it is necessary to obtain high shear stress, low zero-shear viscosity, long-term suspension stability, and strong oxidation resistance.

2.3.1 Raw Materials

Micron-sized carbonyl-iron powder (CC grade, 99.5 %, BASF, Ludwigshafen, Germany) served as the magnetic phase. Sodium hexametaphosphate (AR, Aladdin, China) acted as dispersant, and fumed silica (AR, Aladdin, SSA ≈ 400 $m^2 g^{-1}$) as thixotropic agent. Disodium ethylenediaminetetraacetate (AR, Bide Pharmatech), sodium nitrite (AR, Macklin), anhydrous sodium carbonate (AR, Macklin) and glycerol (AR, Beijing Chemical Plant) served as chelator, preservative, pH buffer and wetting agent, respectively. Cerium-dioxide abrasive (d ≈ 100 nm) was supplied by the Institute of Applied Chemistry, CAS. All solutions were prepared with deionized water (18.2 MΩ cm, JB-80SH system).

2.3.2 Preparation

Sodium hexametaphosphate (0.744 g) was dissolved in de-ionised water (6.47 g) under magnetic agitation. Anhydrous sodium carbonate (0.10 g), disodium ethylenediaminetetraacetate (0.10 g) and glycerol (0.03 mL) were added sequentially and stirred until complete dissolution. Fumed silica (0.20 g) and carbonyl-iron powder (23.4 g, d ≈ 3 μm) were then introduced and the suspension was stirred at 500 rpm for 2 h. Cerium-dioxide abrasive (3.565 g, d ≈ 100 nm) was added last and dispersed at 500 rpm for 30 min. All operations were performed in a sealed vessel to suppress water evaporation and iron oxidation.

2.4 Characterization equipment

Particle topography was imaged with a field-emission SEM (Gemini SEM 300, ZEISS). Powder magnetic properties were recorded at 298 K in a vibrating-sample magnetometer (7307, LakeShore). Rheological data were obtained with a precision rheometer (MCR302, Anton Paar). Post-polish surface quality was quantified by white-light interferometry (NexView, ZYGO).

2.5 Finishing Experiment

Experimental conditions are listed in Table 1. K9 glass blanks (Kodi Saier Optoelectronics, China) were ultrasonically cleaned for 5 min and weighed before each test to reduce error. Every condition was run in triplicate and averaged. Before each run, 30 mL of slurry was sealed, sonicated for 10 min to ensure homogeneity, and used immediately. Removal stability was evaluated at 10 min, 30 min and 60 min. Material removal rate and depth were calculated from：

$$MRR_E = \frac{M_i - M_p}{S \cdot \rho \cdot t} \tag{18}$$

where M_i is the initial mass, M_p the post-polish mass, S the polished area, ρ the workpiece density, and t the polishing duration.

Table 2 Specific Parameters of the Experiment

Workpiece rotational speed(rpm)	Polishing disk rotational speed(rpm)	Machining gap (mm)	Reciprocating speed(mm/min)
300	10	0.6 /0.8 /1.0	130

3. Results and Discussion

3.1 Characterization of MRPF

Fig.4(a)(b) presents SEM micrographs of the carbonyl-iron powder employed in this study. The carbonyl-iron powder is spherical, highly circular and only weakly agglomerated; surface asperities are evident. Fig.4(f) gives a size range of 0.64–3.01 μm, mean 1.80 μm and standard deviation 0.64 μm, indicating a narrow distribution. Figure 4(d) shows the X-ray diffraction pattern of the carbonyl-iron powder; only the α-Fe phase is detected. The hysteresis loop in Fig.4(e) reveals a coercivity of ≈2 Oe and a remanence below 0.2 emu/g^{-1}, confirming near-superparamagnetic behavior. The saturation magnetization is 200.5 emu/g^{-1}, in agreement with the model assumption of ideal soft-magnetic response. As shown in Fig.4(c), obvious flocculent deposits can be observed on the surface of vacuum-dried modified carbonyl iron particles. Combined with the slurry formulation and preparation process, these deposits are mainly fumed silica and adsorbed sodium hexametaphosphate. Such surface coatings optimize the microstructure of magnetic chains and build a stable network in aqueous phase, which leads to a 47% increase in shear stress and a 57% reduction in sedimentation rate of the magnetorheological polishing fluid.

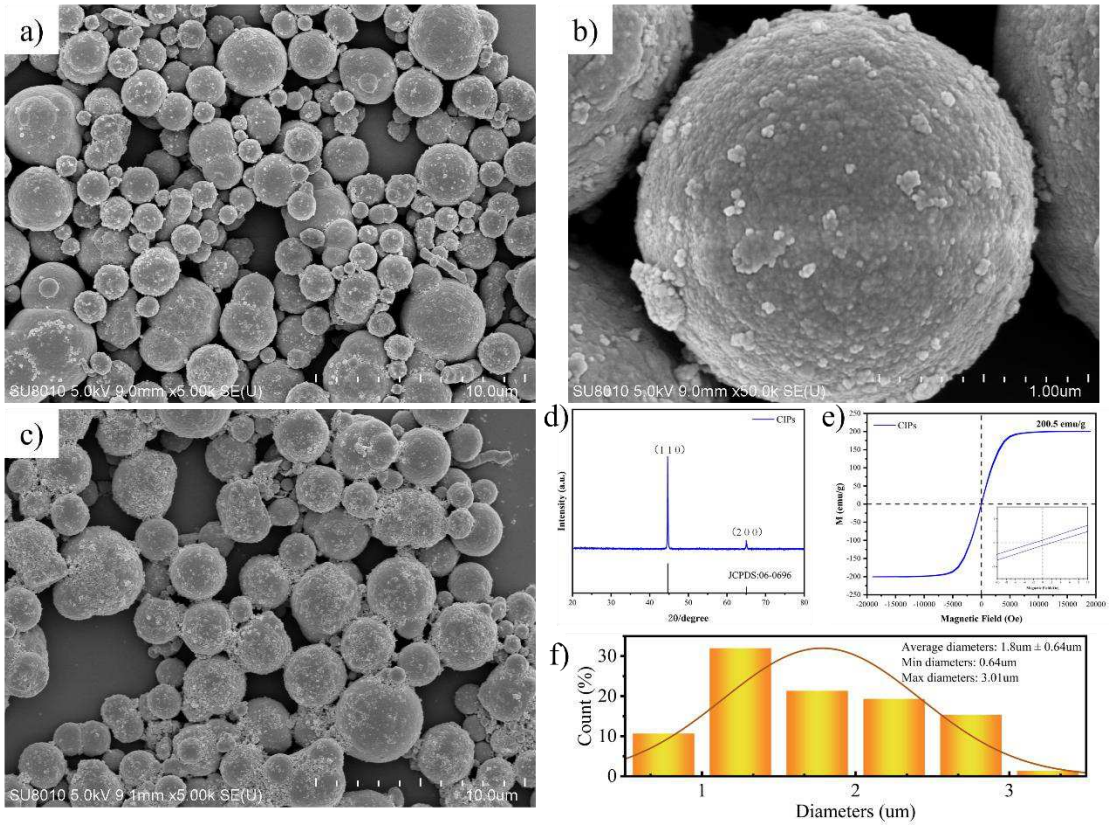

Fig.4. Characterization of CIPs in MRPF (a)(b) SEM of carbonyl-iron powder (c) SEM Image of modified carbonyl-iron powder (d) XRD pattern of carbonyl iron powder (e) VSM pattern of carbonyl iron powder (f) particle size distribution chart of carbonyl iron powder

Fig.5(a) displays shear stress versus magnetic flux density (0–1 T) for the four fluids at a fixed shear rate of 100 s^{-1}. All curves exhibit an initial rapid rise that gradually plateaus, indicating magnetic saturation. Throughout the sweep, MRPF (SHMP+FS) and MRPF (FS) develop higher stresses than MRPF (SHMP) and the additive-free baseline, with the SHMP+FS formulation reaching the maximum. The enhancement is attributed to stronger, defect-poor chain networks: fumed silica adsorbs on the iron surface, fills inter-chain voids and reduces structural flaws, while SHMP dispersion prevents agglomeration, yielding a denser, more load-bearing lattice. As the external field increases, the chains grow denser and aggregate into complex clusters, markedly strengthening the magnetorheological response.

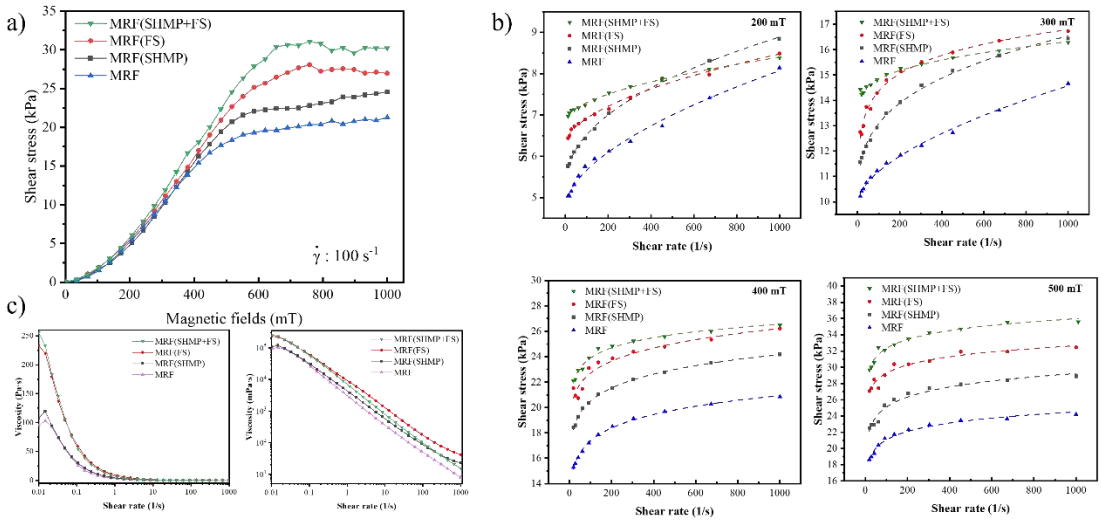

Fig.5. Rheological test results of MRPF with different additives

(a)Shear Stress and Magnetic Field Strength Curve of MRPF

(b) Shear stress-shear rate curves of MRPF under different magnetic fields

(c) Apparent viscosity versus shear rate curve Logarithmic scale is applied to the Y-axis(left); Both the X and Y axes are plotted on logarithmic scales(right).

Fig. 5(b) compares the shear-rate dependence of the four fluids at selected field strengths. Below 300 mT the stresses of the additive-containing slurries are similar and consistently exceed that of the additive-free MRF, corroborating the trend in Fig. 5(a). At 500 mT the curves diverge: the stress rise attenuates with increasing shear rate, yet MRPF (SHMP+FS) still attains 35.6 kPa at 1000 s^{-1}-47 % higher than the 24.2 kPa of the baseline. This gain confirms that the flocculent silica deposits occupy structural defects on and between the iron particles, stiffening the field-induced network.

Fig. 5(c) presents the zero-field viscosity curves of the four slurries as a function of shear rate. All exhibit pronounced shear thinning. Owing to the fumed-silica network, MRPF (SHMP+FS) and MRPF (FS) display apparent viscosities at $\dot{\gamma} < 10$ s^{-1} that are markedly higher than those of MRPF (SHMP) and the additive-free baseline. As $\dot{\gamma}$ increases, the network is progressively disrupted and the viscosities of all four fluids converge to $\eta \lesssim 200$ mPa·s. To quantify this behavior, the shear-thinning coefficient r_s is defined as:

$$r_s = \frac{\eta_{max}}{\eta_{min}} \tag{2}$$

where $\eta_{max}\eta_{max}$ and η_{min} denote the maximum and minimum apparent viscosities, respectively.

Table 2 summarizes the baseline rheological parameters measured at zero field. At 0.1 s^{-1} the maximum apparent viscosity of MRF (SHMP+FS) reaches 53.7 Pa·s—twice that of additive-

free MRPF (25.8 Pa·s)—owing to the silica network. Although MRPF (SHMP+FS) and MRPF (FS) exhibit comparable η<sub>, the minimum viscosity of the former at 100 s^{-1} is 64 % lower than that of MRPF (FS), confirming that sodium hexametaphosphate counteracts the silica-induced thickening and restores flowability close to the MRPF (SHMP) level. The shear-thinning index follows the same trend: single additives weaken the response by roughly one third, whereas the combined system restores the native value of the unmodified fluid. Consequently, the joint addition of sodium hexametaphosphate and fumed silica yields a slurry that retains pronounced shear thinning while keeping the zero-shear viscosity low, providing an compromise between process stability and mobility.

Table 2 Basic properties of magnetorheological fluids with different additives

SHAMP	FS	0.1/s η_{max} (Pa·s)	100/s η_{min} (mPa·s)	r_s
✓	✓	53.7	110	488.2
×	✓	58.5	183	319.7
✓	×	29.6	92	321.7
×	×	25.8	53	486.8

Fig.6 presents the 42-h sedimentation profiles of the four fluids. The final solid volume fractions are 41.4 % (MRPF), 40 % (MRPF-SHMP), 21.1 % (MRPF-FS) and 17.5 % (MRPF-SHMP+FS); the last value corresponds to 43.8 % of the additive-free baseline. Linear regression of the first 3 h (inset) gives the initial settling rate k; MRF-SHMP+FS displays a slope that is only 21 % of the unmodified value, confirming that the combined dispersant and thixotropic agent provides the most effective steric and viscous stabilization.

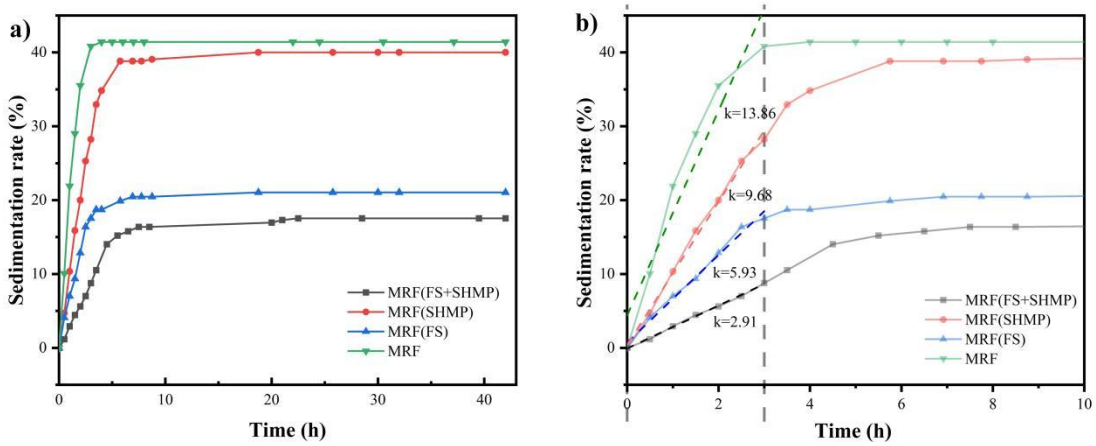

Fig.6 Sedimentation curve of MRPF

3.3 Discussion on the Validation and Polishing Results of the Material Removal Model

Three parameters —machining gap, disc speed, workpiece speed and reciprocating speed— were screened; machining gap was previously identified as the dominant factor in our research[14]. To probe both accuracy and temporal stability, clearance and dwell time were therefore varied while the remaining variables were fixed. Figure 7(a) compares the theoretical and measured removal rates for the final triplet. During the first 30 min the model predicts the profile within 5 % error and the surface finishes well (Sa = 1.56 nm, Figure 6(b)). Beyond 30 min the discrepancy grows four-fold by 180 min and the removal function becomes unreliable. Comet tails appear after 60 min (Figure 7(c)); extensive tails and deep localized scratches dominate at 180 min (Figure 7(d)), driving Sa to 3.59 nm and 6.03 nm, respectively.

As illustrated in Fig. 7(a), an intriguing dynamic crossover behavior in MRR deviation can be observed between the short-term (30 min) and long-term (180 min) polishing stages under different machining gaps. At the early stage, the MRR deviation is most pronounced at the 0.6 mm gap. This is attributed to the fact that a smaller machining gap induces a significantly higher shear rate and intense localized frictional heating within the polishing zone. This accelerated the initial evaporation of deionized water, leading to a rapid rise in MRPF concentration and an early departure from the theoretical baseline model. However, at the late stage, the deviation at the 1.0 mm gap surpasses that of the 0.6 mm gap and becomes the highest. By this extensive duration, the bulk water across the wide disk surface has largely evaporated under the conventional configuration. Under such starved conditions, the strong magnetic field gradient at the 0.6 mm gap can still tightly constrain the dry iron chains to maintain residual contact with the workpiece. Conversely, at the 1.0 mm gap, the magnetic excitation is significantly weaker due to the increased distance from the magnetic pole. The weak field fails to stabilize and hold the dried slurry, causing the three-body wear paradigm to completely collapse and yielding the massive MRR divergence. This dynamic transition demonstrates that while smaller gaps suffer from faster initial thermal degradation, larger gaps are more susceptible to complete magnetic confinement failure during long-term operations. A circulating device incorporating a recovery section, a replenishment section, and an effluent section should be designed.

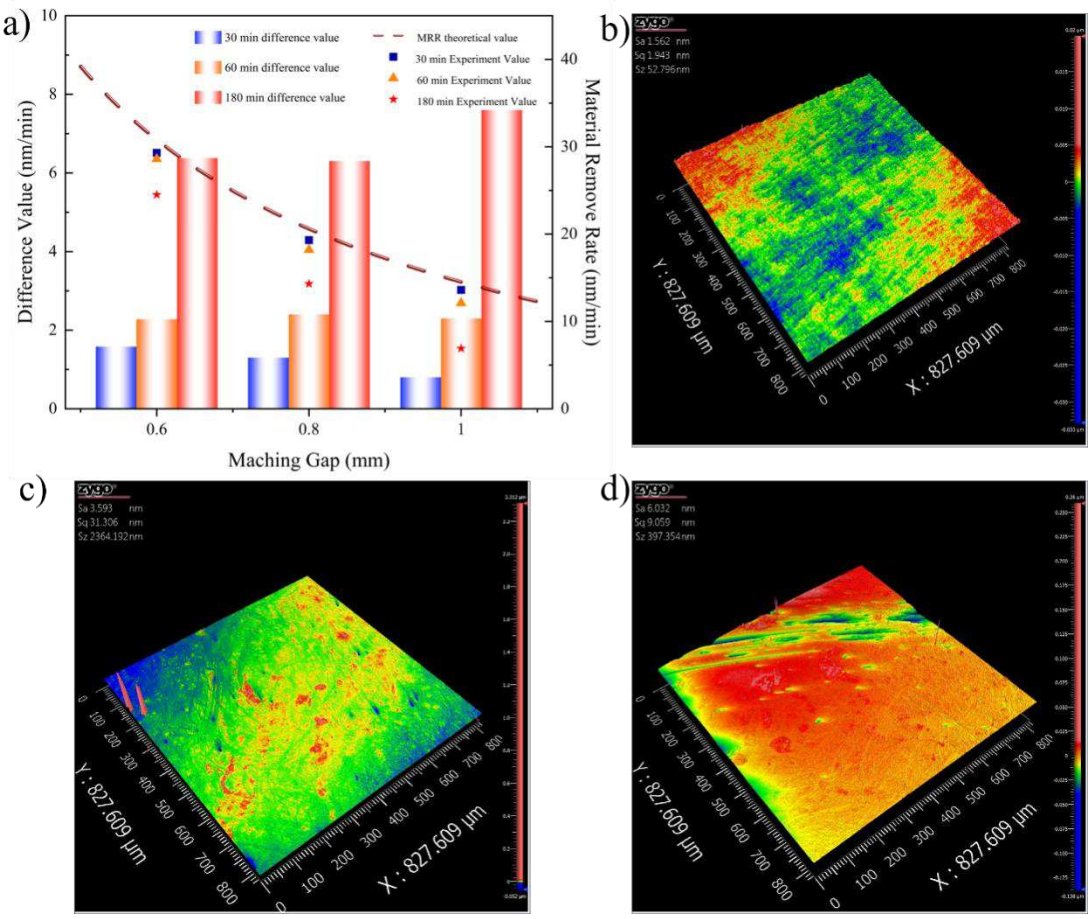

Fig.7 Polishing removal effect verification diagram (a)Deviation diagram between theoretical and measured material removal rates for different processes and processing times (b)(c)(d) WLI surface maps of workpieces processed for 30 min, 60 min and 180 min

4. Design of a Reciprocating RDMRF Recycler

RDMRF complicates slurry recovery: prolonged field exposure destabilizes any ferrofluid, and MRFs—having the highest solids loading—are the most vulnerable. Conventional layouts therefore restrict the strong field to the active zone so the slurry reverts to "ordinary" behavior once it leaves the magnet gap. Reciprocation of the workpiece spindle, however, compresses the exiting MRF into a thin, wide film that remains magnetized long enough to hinder suction-based return. The enlarged air–fluid interface is the principal cause of the eight-fold drift in removal rate after 30 min. Non-contact pick-up cannot collect the dilute film completely, whereas contact scrapers abrade the disc and introduce debris into the slurry. Published design concepts of recovery are almost exclusively wheel-type [24-27]; disc systems remain largely unexplored. A magnetically tunable, plug-in module capable of handling high slurry flow rates is therefore essential for reliable operation of reciprocating-disc MRF platforms.

4.1 Integrated Recycler Design

Fig.8 shows the collector conceived to meet the above requirements. It integrates three functional zones: an electromagnet, a flow guide, and a negative-pressure pick-up. The electromagnet comprises a roof panel, inner and outer shells of high-permeability alloy, and an annular coil. When energized, flux runs axially and closes through the shell assembly; the downward extension of the shells forms a narrow annular gap that intentionally leaks flux into the air gap. This leakage creates a magnetic seal that stops the MRPF film and causes a local "liquid dam"; the seal strength is tuned by the coil current. A baffle limits the dam height to keep fluid away from the coil. The arrested slurry is drawn into a central port at the gap floor by a peristaltic pump, conveyed to an external reservoir, re-diluted under ferrous-hydroxide feedback from a vortex sensor, mixed, and finally re-injected onto the disc, closing the loop.

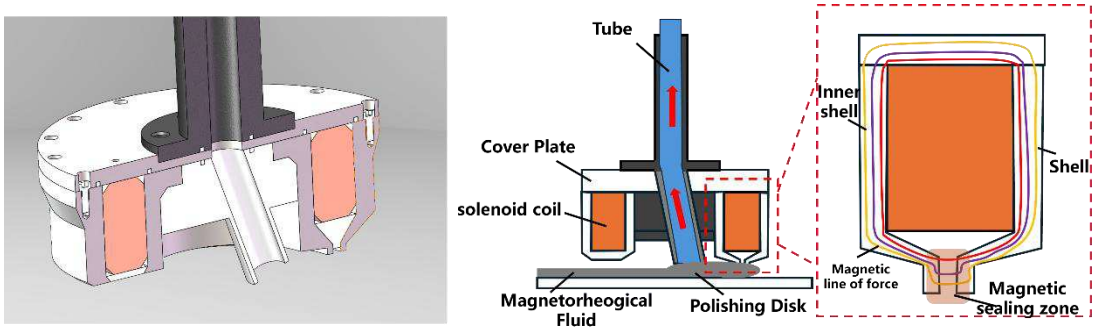

Fig.8 3D sectional view and operating principle of the recycler

4.2 Seal load-capacity analysis

Analogous to conventional ferrofluid seals, the magnetic barrier created by the leakage field in the collector must continuously withstand the impact of the oncoming slurry. Under a high magnetic field the MRPF behaves as a Bingham visco-elastic solid; the seal must therefore immobilize the fluid and provide adequate strength to arrest the flow of the following slurry.

To maintain the MR fluid in a semi-solid state throughout the machining cycle, the magnetic body force within the gap must exceed the hydrodynamic load, requiring a field gradient that fulfils[28]：

$$\mu_0 MV gradH > \rho v Q \tag{18}$$

Here ρ is fluid density, v velocity, Q flow rate, M magnetization, V sealed volume and $gradH$ field gradient; under maximum disc speed and flow the criterion is met at 30 kA m^{-1}. Under the most severe operating envelope—maximum disc speed and maximum slurry flow—the sealing criterion is satisfied at a field of only 30 kA m^{-1}.

4.3 Magnetic-circuit design and analysis

Once the MR fluid's saturation magnetization and rheology are fixed, seal reliability is governed solely by the leakage field. To maximize versatility, this field must be tunable over

the widest possible range. The on-axis strength of a short, single-layer, closely wound hollow solenoid (equal turns per layer) is：

$$H = \frac{nIL_c}{2} \cdot ln \frac{r_1 + \sqrt{r_1^2 + \left(\frac{L_c}{2}\right)^2}}{r_2 + \sqrt{r_2^2 + \left(\frac{L_c}{2}\right)^2}} \tag{19}$$

where n is the turn density, I the excitation current, L_c the coil length, r_1 the outer radius and r_2 the inner radius. For given geometry the centre field is therefore set only by the turn density and the excitation current. Because the maximum continuous current is limited by wire cross-section, 0.8 mm enamelled copper was selected to provide the widest adjustable range without overheating.

Electromagnetic performance of the recycler was analyzed with COMSOL Multiphysics. Because the seal demands a high field while the inlet must remain virtually field-free, the geometry was split into two 2-D axisymmetric domains that were solved separately to reduce computation. Material data are given in Table 3. With direct-current excitation, eddy-current and skin effects are absent, so a fine unstructured mesh was used. The computed flux density is plotted in Fig.9. Lines are dense in the high-permeability shell assembly and leak symmetrically through the lower slit, forming the seal zone; the upper leakage is shunted by the flow guide and plays no sealing role. Horizontal cutlines 0.5 mm, 1 mm and 1.5 mm below the slit (Fig.9(e) shows the 1.5 mm trace) give 29.2 kA/m on the slit axis—above the 30 kA/m requirement of Section 4.2. Conversely, a vertical trace 5 mm beneath the inlet (Fig.9 a–c) shows the field has already fallen below 8 kA/m, so the slurry remains liquid and inlet clogging is avoided.

Table 3 Structural materials and their properties used in the finite-element simulation

Structures	Materials	Relative magnetic permeability	Electrical Conductivity
Inner shell	Iron	4000	1.12e7
Outer	Iron	4000	1.12e7
Coil	Copper	1	5.998e7
Roof panel	Iron	4000	1.12e7
Domain of definition	Air	1	0

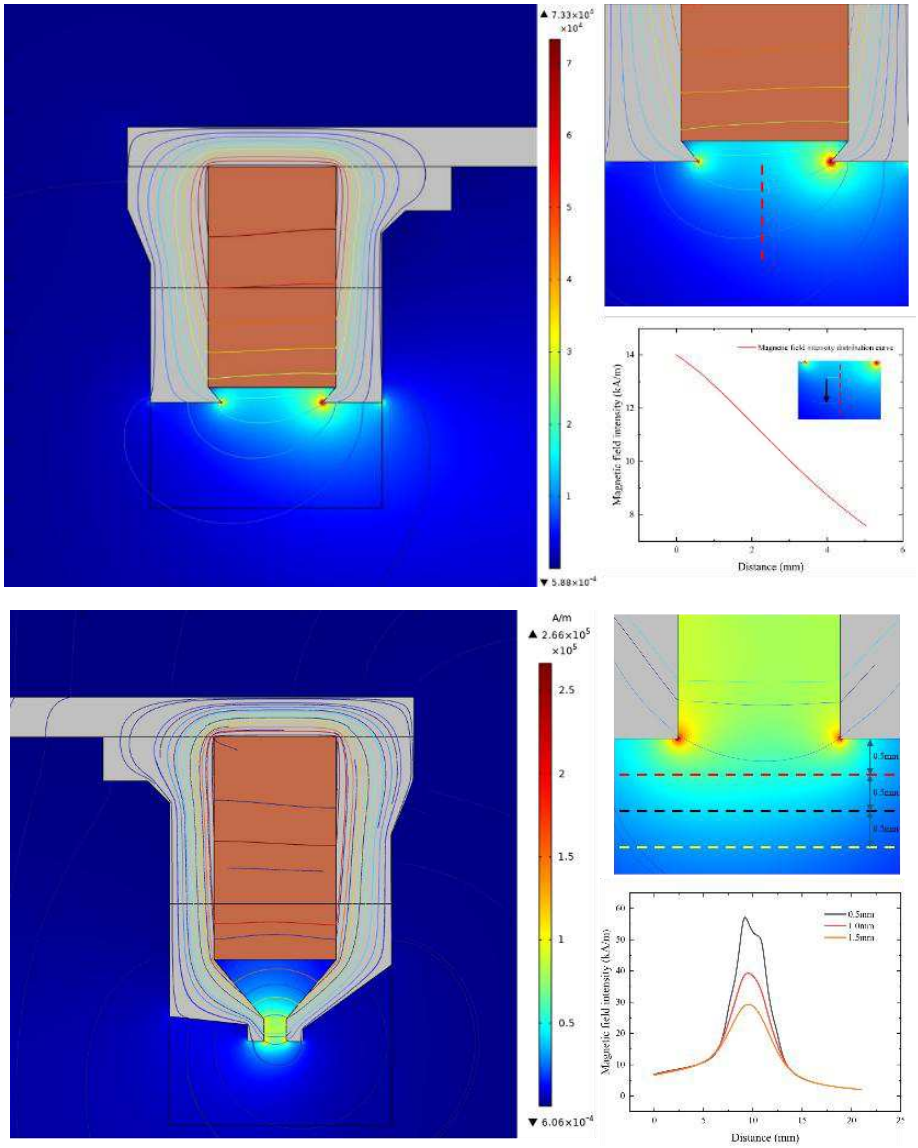

Fig.9 COMSOL Magnetic Field Simulation and Analysis Diagram

(a)(b) Magnetic field cloud map at inlet (c) Magnetic field value diagram at 5mm below the center point of the inlet notch (d)(e) Magnetic Field Cloud Map of the Sealed Zone

(f) Magnetic field value diagram 0.5mm 1mm 1.5mm below sealing zone level

4.4 Recycling effect verification

The recycler was fixed 1 mm above the disc surface with its drainage port aligned to the rotation direction and energized at 0.5 A dc. A peristaltic pump withdrew 2000 ml/min-four times the process flow-through a single hose. After 12 h continuous run, no seal failure was detected, even during start-up and shut-down transients. The polishing Halbach array remains stationary and the disc rotates at 10 rpm. Within 180 min of operation, the loop compensates water evaporation and inhibits particle sedimentation, keeping MRPF composition stable. Recycler temperature remained below 30 °C, leaving the MRPF unaffected; the flow sheet is given in

Fig.10.

Fig.10 RDMRF processing zone (left); recycling zone (right)

5. MRR stability validation experiment

The effect of evaporation on the removal function of the water-based MR fluid was verified with the recycler under the conditions of Section 4.3. To rigorously evaluate the engineering value of our newly designed slurry loop recycler under the most critical scenarios , we selected the 0.6mm gap—which suffers from the most aggressive initial thermal/evaporative drift.

The effect of evaporation on the removal function of the water-based MR fluid was verified with the recycler under the conditions of Section 4.3 (machining gap 0.6 mm). Three test groups were run: (1) no recovery, (2) recovery with the peristaltic pump feeding the reclaimed MR fluid into a beaker where a vortex sensor measured carbonyl-iron content and water was replenished while the mixture was continuously stirred, then returned to the disc via the outlet line and nozzle, and (3) recovery with the reclaimed fluid discarded and only fresh slurry sprayed through the nozzle. Workpieces were processed for 30 min, 60 min and 180 min and the material removal rate versus time was plotted. The figure shows severe removal-function distortion without circulation, consistent with the findings reported in Section 4. With circulating water make-up and agitation, the removal function remained stable: evaporative loss was offset, preserving the original liquid volume fraction, while continuous flow prevented sedimentation of magnetic and abrasive particles, suppressing removal-rate fluctuations caused by concentration stratification. Nevertheless, stability still lagged behind the fresh-slurry control, and the gap widened to 8 % after 180 min. The principal reason is the interfacial reaction between CeO_2 abrasives and SiO_2 in K9 glass, which forms Si–O–Ce bonds and lowers the particles' chemical reactivity. These effects progressively shift the circulating system away from its initial state and produce the observed 8 % deviation. Fig. 11(b) and (c) present the as-received surface and the 180-min finish obtained with the recycler in place. Continuous polishing for 3 h yielded Ra 1.480 nm and Sa 1.519 nm—values indistinguishable from the 30-min reference in Section 3.2—confirming that recycler integration sustains optical-grade

finishes throughout prolonged RDMRF campaigns.

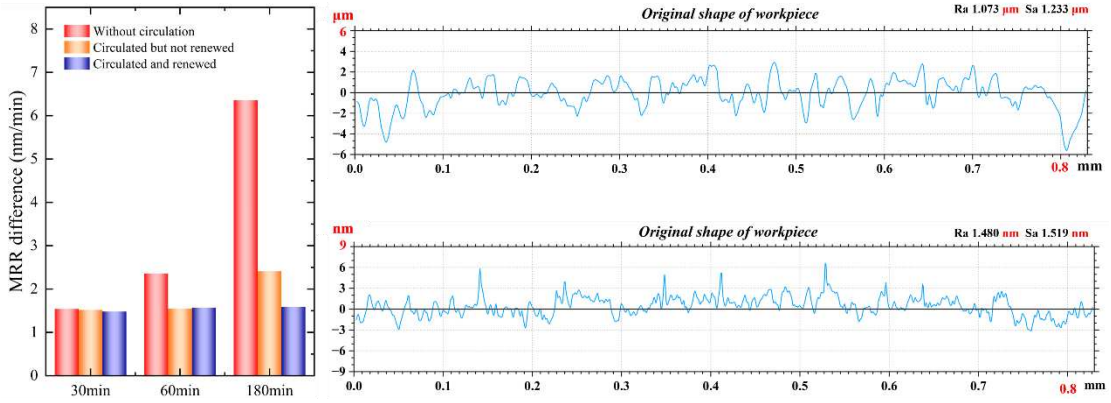

Fig.11(a) Error plot for removal efficiency of three sets of experimental material

(b) Initial state of the workpiece and 2D roughness scan diagram after 180 minutes of machining in the second experimental group.

6. Conclusion

Our study focus the dual demands for high precision and high efficiency in the ultra-precision machining of optical mirrors and semiconductor wafers for industrial production. The main conclusions are below:

(1) A highly stable MRPF with high shear strength and low zero-shear viscosity was prepared. By adding SHAMP and fumed silica, shear stress increased by 47% and sedimentation rate decreased by 57%. This polishing fluid closely approaches the ideal assumption of the removal function.

(2) The removal function mathematical model was validated using a highly stable magnetorheological polishing fluid. For the first time, both the accuracy and long-term stability of the removal function were comprehensively considered. It was found that within the first 30 minutes of processing, the removal function error was less than 5%. However, when the processing time was extended to 180 minutes, the error increased fourfold, causing the surface quality to deteriorate from Sa 1.562 nm to Sa 6.032 nm, with comet-tail defects appearing on the surface. Analysis indicates that the primary causes are water evaporation and particle sedimentation.

(3) A RDMRF non-contact stray magnetic field recovery device has been designed. This recovery device enables stable recovery without heat dissipation during continuous 12-hour processing, overcoming the limitation that conventional disc-type magnetorheological polishing cannot recover stray magnetic fields. It allows disc-type magnetorheological polishing to achieve a smooth surface with Sa 1.519 nm and Ra 1.480 even under extended

processing times of 180 minutes.

(4) Even after the recycler eliminated sedimentation and evaporation, an 8 % deviation in removal rate persisted at 180 min. This residual error is traced to Si–O–Ce bonds formed on the CeO_2 abrasive surface, which lower its chemical activity and enrich the slurry with fine grinding debris. The finding identifies the ultimate factor that presently limits further gains in removal stability and surface quality.

Funding

This study was Supported by the Fundamental Research Funds for the Central Universities (2024JBZY027).

Data availability

The data that support the findings of this study are available on request from the corresponding author, upon reasonable request.

Declaration of Interest Statement

The authors certify that the manuscript has not been previously published by any of the authors and it is not under consideration for publication elsewhere. All authors have seen and approved the submission of this manuscript.

References：

[1] Zhang Y B, Tang X Y, Yuan H, et al. Systematic investigation on the performance and reliability of 4H-SiC mosfets with nonkiller epitaxial morphological defects [J]. Ieee Transactions on Electron Devices, 2025, 72(5): 2492-2498.

[2] Lipton J, Yurash B, Sorensen A, et al. Low-loss nanophotonic devices with chip-level uniformity and integrated color centers in an SiC-on-insulator [J]. Acs Photonics, 2025, 12(5): 2397-2405.

[3] Song DL, Du HG, Lin JQ, Zhou XQ, Wang RQ. A review on magnetorheological jet polishing technique for microstructured functional surfaces. Lubricants 2022;10: 237.

[4] Sammer T, Shi XY, Khan MZ, Matkovic A, Teichert C, Raith JG. Influence of broad ion beam polishing on the surface roughness of hydrated cement paste and its implications on microstructural analysis. Cem Concr Res 2024;182:107555.

[5] Kordonski W, Golini D. Magnetorheological suspension-based high precision finishing technology (MRF) [J]. Smart Materials and Structures, 1999, 4(1): 275-281.

[6] Rajput A S, Das M, Kapil S. A comprehensive review of magnetorheological fluid assisted finishing processes [J]. Machining Science and Technology, 2022, 26(3): 339 376.

[7] Shorey A B, Kwong K M, Johnson K M, et al. Nanoindentation hardness of particles used in magnetorheological finishing (MRF) [J]. Applied Optics, 2000, 39(28): 5194 5204.

[8] Kumar J S, Paul P S, Raghunathan G, et al. A review of challenges and solutions in the preparation and use of magnetorheological fluids [J]. International Journal of Mechanical and Materials Engineering, 2019, 14(1): 13.

[9] Yan Q S, Yan J W, Lu J B, et al. Ultra smooth planarization polishing technique based on the cluster magnetorheological effect [J]. Surface Finishing Technology and Surface Engineering Ii, 2010, 135: 18-23.

[10] Ren K, Luo X, Zheng L, et al. Belt-MRF for large aperture mirrors[J]. Optics Express, 2014, 22(16): 19262-19276.

[11] Pan J, Yan Q. Material removal mechanism of cluster magnetorheological effect in plane polishing[J]. The International Journal of Advanced Manufacturing Technology, 2015, 81(9): 2017-2026.

[12] Bai Z, Yan Q, Lu J, et al. Parametric investigation into accommodate-sinking effect of cluster magnetorheological effect pad[J]. The International Journal of Advanced Manufacturing Technology, 2014, 75(9): 1447-1456.

[13] Lu J, Yan Q, Tang A, et al. Simulation analysis and structure optimization of the polishing disc with the tiny-grinding wheel cluster based on MR effect[C]//5th International Symposium on Advanced Optical Manufacturing and Testing Technologies: Advanced Optical Manufacturing Technologies. SPIE, 2010, 7655: 222-227.

[14] Jiang J, Zhang Z, Tao M, et al. Analysis and experimental study on influencing factors to magnetorheological finishing for ultra-precision optical mirror surfaces[J]. Proceedings of the Institution of Mechanical Engineers, Part B: Journal of Engineering Manufacture, 2025: 09544054251359857.

[15] Guo H, Wu Y, Lu D, et al. Effects of pressure and shear stress on material removal rate in ultra-fine polishing of optical glass with magnetic compound fluid slurry[J]. Journal of Materials Processing Technology, 2014, 214(11): 2759-2769.

[16] Guo H, Wu Y. Ultrafine polishing of optical polymer with zirconia-coated carbonyl-iron-particle-based magnetic compound fluid slurry[J]. The International Journal of Advanced Manufacturing Technology, 2016, 85(1): 253-261.

[17] Ghai V, Ranjan P, Batish A, et al. Atomic-level finishing of aluminum alloy by chemo-mechanical magneto-rheological finishing (CMMRF) for optical applications[J]. Journal of Manufacturing Processes, 2018, 32: 635-643.

[18] Shao L, Yuan Z, Duan S, et al. Material removal function of deterministic shear thickening polishing using wedge structure polishing tool[J]. Journal of Manufacturing Processes, 2025, 149: 573-590.

[19] Buijs M, Korpel-van Houten K. A model for lap** of glass[J]. Journal of materials Science, 1993, 28(11): 3014-3020.

[20] Buijs M,Houten KKV(1993)Three-bodyabrasion of brittle mate rials as studied by lapping. Wear 166(2):237–245. doi:10.1016/ 0043-1648(93)90267-P

[21] Mulik, Rahul S., and Pulak M. Pandey. "Experimental investigations and modeling of finishing force and torque in ultrasonic assisted magnetic abrasive finishing." (2012): 051008.

[22] Lu, Mingming, et al. "Modelling and process analysis of material removal rate in magnetorheological polishing of fused quartz glass." *Journal of the Brazilian Society of Mechanical Sciences and Engineering* 47.10 (2025): 471.

[23] Yang, Peiran. "Numerical analysis of fluid lubrication." *National Defense Industry Press, Beijing* (1998).

[24] Jacobs S D , Kordonski W , Prokhorov I V , et al. Deterministic magnetorheological finishing: US, US5795212 A[P]. 1998.

[25] Kordonski W , Hogan S , Sekeres A . Magnetic wiper: US, US6309285 B1[P].

[26] Kordonski W , Price A , Carapella J , et al. Method and apparatus for forming a dynamic magnetic seal using magnetorheological fluid: US, US7156724 B2[P]. 2007.

[27] Niu ZY, Wu JB, Zeng JC. Design of an Electromagnetic-Based Magnetorheological Polishing Fluid Recycler [J]. Mechanical Design,2023,40(07):1-7.

[28] Kordonski W , Golini D . Multiple Application of Magnetorheological Effect in High Precision Finishing[J]. Journal of Intelligent Material Systems and Structures, 2002, 13(7):401-404.